Mergers of binary neutron stars with realistic spin

Sebastiano Bernuzzi and Tim Dietrich

Theoretical Physics Institute, University of Jena, 07743 Jena, Germany

Wolfgang Tichy

Department of Physics, Florida Atlantic University, Boca Raton, Florida 33431, USA

Bernd Brügmann

Theoretical Physics Institute, University of Jena, 07743 Jena, Germany

Simulations of binary neutron stars have seen great advances in terms of physical detail and numerical quality. However, the spin of the neutron stars, one of the simplest global parameters of binaries, remains mostly unstudied. We present the first fully nonlinear general relativistic dynamical evolutions of the last three orbits for constraint-satisfying initial data of spinning neutron star binaries, with astrophysically realistic spins aligned and antialigned to the orbital angular momentum. The initial data are computed with the constant rotational velocity approach. The dynamics of the systems is analyzed in terms of gauge-invariant binding energy vs orbital angular momentum curves. By comparing to a binary black hole configuration, we can estimate the different tidal and spin contributions to the binding energy for the first time. First results on the gravitational waveforms are presented. The phase evolution during the orbital motion is significantly affected by spin-orbit interactions, leading to delayed or early mergers. Furthermore, a frequency shift in the main emission mode of the hypermassive neutron star is observed. Our results suggest that a detailed modeling of merger waveforms requires the inclusion of spin, even for the moderate magnitudes observed in binary neutron star systems.

I. INTRODUCTION

Neutron stars in binaries are spinning objects [1]. The most famous example is the double pulsar PSR J0737-3039, for which the orbital period and both spin periods, as well as both spin-down rates, are known [2]. The faster-spinning pulsar in this system has a spin period of $P = 22.70$ ms (PSR J0737-3039A) [3], which corresponds to a dimensionless spin of $\chi \sim 0.02$ [4–7]. This is the fastest-spinning pulsar in a binary system observed so far. From the orbital period we can estimate that this system will merge in about 85 My due to emission of gravitational waves (GWs). Over this time period, the faster spin will decrease by only about 20% if we assume spin-down is due to magnetic dipole radiation [4]. Thus, we do expect spin effects near merger, even though the other spin is much smaller and plays no big role for this system.

A value of $\chi \sim 0.02$ may appear rather small. For black hole systems, $\chi \leq 1$ is expected to approach 1 in some cases. A theoretical limit for isolated neutron stars described by a large class of nuclear equations of state (EOSs) and uniform rotation is $\chi \sim 0.7$ [8]. Configurations with $\chi > 1$ are, however, possible if, for example, differential rotation is allowed, e.g. Ref. [9]. It is not clear whether or how many of these large-spin single neutron stars can be found in binaries. Theoretical limits for neutron stars in binaries depend on the mechanism of binary formation and binary history and are difficult to predict precisely [1]. Given that the observed neutron star spin in binaries is comparatively small, star rotation is often ignored when modeling likely astrophysical neutron star mergers.

Binary neutron stars (BNSs) are a primary source of GWs. Advanced interferometric configurations in LIGO and Virgo experiments are expected to detect from 0.4 to 400 events per year, starting from 2018–2019 (or even from 2016) [10,11]. At the expected sensitivities, neglecting spin effects in template-based searches of BNSs can lead to substantial losses in the matched-filter signal-to-noise ratio for the inspiral [6,12]. Template waveforms of the inspiral phase that cover most of the relevant frequency band are typically constructed with post-Newtonian approximants. However, of particular interest is also the detection of the late-inspiral-merger waveforms, because such signals can be used to constrain the high-density equation of state of neutron stars [5,13,14]. Differently from the inspiral case, precise merger waveforms can be constructed only by means of numerical relativity simulations, e.g. Refs. [15–18].

Although spin is one of the elementary parameters of a binary system, most studies of BNSs to date have not considered neutron stars with realistic rotation. Almost all BNS simulations have started from initial data which have been constructed as (quasiequilibrium) stationary solutions

in circular orbits, within either the corotational [19–21] or the irrotational [22–27] approach. There is spin in the corotational case, but it is determined by the orbital period and describes an unrealistic configuration because of the low viscosity of neutron star matter [28].

Numerical simulations of BNS mergers in full general relativity have reached a high degree of precision and detail. Recent developments include radiation transport [29], microphysical equations of state [30], and nonideal magnetohydrodynamics [31], as well as highly eccentric mergers [32,33]. See Ref. [34] for a review and more references. In all these simulations the Einstein equations are solved without any approximation as a $3 + 1$ evolution system for a given initial configuration. Most BNS simulations have focused on irrotational configurations. In this case the stars' spin is neglected and not modeled in the simulations. A way to construct quasiequilibrium BNS initial data in circular orbits with spins has been recently proposed in Refs. [4,35]. The *constant rotational velocity* (CRV) formalism developed there is, to date, the only consistent method to produce realistic initial data for BNS mergers with spins (see Refs. [36,37] for earlier approximate approaches).

In this work, we report dynamical evolutions of BNS initial data constructed with the CRV approach. We study the dynamics of the last three orbits, merger and postmerger phase, of equal-mass BNS configurations with spins aligned or antialigned to the orbital angular momentum. The rotational period of each star is moderate and compatible with astrophysical observations. We propose two simple ways to estimate the dimensionless spins of the binary and show that both agree within ~10%. The dynamics and gravitational radiation emitted are systematically compared with an irrotational configuration with the same rest mass. The orbital evolution is studied by means of gauge-invariant binding energy vs orbital angular momentum curves [38]. We compare these curves with a binary black hole simulation and with analytical models, show the consistency of the results, and extract the different contributions to the binding energy from spin and tidal interactions. The merger remnant is also investigated, focusing in particular on the effect of rotation on the hypermassive neutron star.

Our results are the fundamental first step towards the use of CRV initial data for modeling rotating stars in BNS mergers. In particular, we show that even moderate spins have a significant impact on the merger dynamics and on the gravitational radiation emitted. Numerical relativity simulations aiming at an accurate description of the gravitational waves emitted by these sources should take into account the rotation of the star.

General relativistic evolution of spinning neutron stars has been considered for a long time in the corotational approach, both in full general relativity and in the conformally flat approximation; see e.g. Refs. [39,40] and Ref. [34] for other references. More recently, alternative approaches have been proposed in Refs. [41,42]. Both

works employ constraint-violating initial data produced by superposing either two boosted single-star configurations or an arbitrary velocity pattern. Such data violate both Einstein constraints and some hydrodynamical stationarity conditions. It is unclear how these initial data relate with the ones used in this work. Thus, in the following, we do not attempt a direct comparison of the results, but just point out certain similarities.

The paper is organized as follows: In Sec. II we review main aspects of the initial data and describe how to estimate the spin of our configurations. The numerical method is summarized in Sec. III. The dynamics of the numerical evolutions is analyzed in Sec. IV by considering (i) the analysis of the orbital motion with binding energy vs orbital angular momentum curves, and (ii) the postmerger phase and a mode analysis of the hypermassive neutron star in the merger remnant. Gravitational radiation is discussed in Sec. V. We conclude in Sec. VI.

Dimensionless units $G = c = M_\odot = 1$ are employed hereafter; physical units are sometimes explicitly given in the text for clarity.

II. EQUILIBRIUM CONFIGURATIONS

A. A review of the CRV approach

The initial data used here are constructed using the CRV method [4,35]. For this method we use the Wilson-Mathews approach [43,44], which is also known as conformal thin sandwich formalism [45], for the metric variables together with certain assumptions. The first assumption is the existence of an approximate helical Killing vector ξ^μ, such that

$$\pounds_\xi g_{\mu\nu} \approx 0. \tag{1}$$

We also assume similar equations for scalar matter quantities such as the specific enthalpy h. However, the 4-velocity u^μ is treated differently, and it is not assumed that $\pounds_\xi u^\mu$ vanishes. Instead we write

$$u^\mu = \frac{1}{h}(\nabla^\mu \phi + w^\mu), \tag{2}$$

where $\nabla^\mu \phi$ and w^μ are the irrotational and rotational parts of the fluid velocity. We then assume that

$$\gamma_i^\nu \pounds_\xi (\nabla_\nu \phi) \approx 0, \tag{3}$$

so the time derivative of the irrotational piece of the fluid velocity vanishes in corotating coordinates. We also assume

$$\gamma_i^\nu \pounds_{\frac{\nabla\phi}{hu^0}} w_\nu \approx 0 \tag{4}$$

and

$$^{(3)}\pounds_{\frac{w}{hu^0}} w_i \approx 0, \tag{5}$$

TABLE I.   BNS configurations considered in this work. All initial data are for equal mass configurations, where each star has a baryonic mass $M_b = 1.625$. The polytropic exponent and constant are $\Gamma = 2$ and $K = 123.6489$. Spins are aligned or antialigned to the orbital angular momentum. The columns contain the following information: the name of the configuration, the rotational part of the fluid velocity given in terms of the angular velocity ω^z, the ADM mass and ADM angular momentum of the binary, the gravitational mass M_s of a single star in isolation, the spin S_s of an isolated star with the same ω^z and M_b, and the corresponding dimensionless spin χ_s, the spin estimate S using the irrotational configuration as a reference point, and the corresponding dimensionless spin χ. Γ configurations are evolved with Γ-law EOSs; P configurations are evolved with the polytrope (barotropic evolutions).

Name	ω^z	M_{ADM}	J_{ADM}	M_s	S_s	χ_s	S	χ
Γ_{050}^{--}	-0.00230	2.99932	8.69761	1.51496	-0.11449	-0.0499	-0.10224	-0.0419
Γ_{025}^{--}	-0.00115	2.99911	8.79949	1.51487	-0.05710	-0.0249	-0.05130	-0.0198
Γ_{000}^{--}	0.00000	2.99903	8.90209	1.51484	0.00000	0.0000	0.00000	0.0000
Γ_{025}^{++}	0.00115	2.99907	9.00585	1.51487	0.05710	0.0249	0.05188	0.0252
Γ_{050}^{++}	0.00230	2.99926	9.11092	1.51496	0.11449	0.0499	0.10442	0.0480
P_{100}^{--}	-0.00460	3.00012	8.49472	1.51533	-0.23128	-0.1007	-0.20368	-0.0861
P_{000}	0.00000	2.99903	8.90209	1.51484	0.00000	0.0000	0.00000	0.0000
P_{100}^{++}	0.00460	2.99993	9.32688	1.51533	0.23128	0.1007	0.21240	0.0950

which describe the fact that the rotational piece of the fluid velocity is constant along the world line of the star center. These latter two assumptions lead to the name "constant rotational velocity method."

For the data considered here, we set

$$w^i = \epsilon^{ijk}\omega^j(x^k - x_{C*}^k), \qquad (6)$$

where x_{C*}^i is the center of the star (defined as the point with the highest rest-mass density) and where ω^i is an arbitrarily chosen angular velocity vector. In Ref. [35] we have verified that this specific choice leads to only a negligible shear, so that we can avoid any substantial differential rotation.

This method is implemented in the SGRID code [46–48], which is used to construct the initial data. We then import these data into the BAM code (see below) by spectral interpolation onto BAM's grid points.

B. Selected configurations

The initial configurations considered in this work are $\Gamma = 2$ polytropes, $p = K\rho^\Gamma$, with $K = 123.6489$, individual rest mass (or baryonic mass) $M_b = 1.625$, and different rotational states. Table I summarizes the main properties of the models. The rotation state of each star is characterized by its angular velocity ω^i. For the simulations described here, we have chosen ω^i to point along the z direction, with the values given in Table I. If we use $P = 2\pi/\omega^z$ to define a spin period for each star, the different spinning configurations in Table I correspond to periods of 6.7, 13.4 and 26.9 ms. Notice, however, that these periods are not exactly the spin periods an observer at infinity would measure. As we show in Appendix A, the spin periods observed at infinity are about 10% larger. The initial data employed in this work are selected from equilibrium sequences similar to those computed in Ref. [35]; some details are given in Appendix B.

The individual isolation masses of the irrotational model are $M_{\mathrm{TOV}} = 1.51484$, which is equivalent to the ADM mass of a TOV star with the same rest mass as the binary's individual $M_b = 1.625$. All the binary models have about the same proper separation of $D \approx 40.4$ (59 km). The ADM masses differ by a maximum of 0.04%. The CRV formalism [4,35] allows us to construct single rotating star configurations by assuming that the approximate Killing vector ξ^μ is the timelike Killing vector $\xi^\mu = (1, 0, 0, 0)$. We have thus computed single-star models with half the rest mass of the binary and the same ω^z. Each model is characterized by an ADM mass M_s and an ADM angular momentum S_s. For the nonrotating model, of course, $M_s = M_{\mathrm{TOV}}$ and $S_s = 0$; other values are reported in Table I. We will make use of these values in the following sections. We define $M = 2M_{\mathrm{TOV}}$ and scale the time in the plots with this mass.

Additionally to these BNS configurations, we consider a nonspinning equal-masses binary black hole (BBH) run. The initial configuration is identical to the one in Table III of Ref. [49] with an initial separation of ≈ 11 and an eccentricity of ≈ 0.0002.

C. Spin estimates

In the CRV approach, the natural quantity describing the spinning motion is ω^i; however, in the context of GWs it is convenient to consider "a spin." Since the spin of a single star in a binary is not unambiguously defined in general relativity, we propose here two simple different ways of estimating the spin magnitude S.

A simple method (which to our knowledge is new in this context) is to consider single stars in isolation with the same rest mass and the same ω^z, computed as described in Sec. II B. These stars have a well-defined angular momentum S_s. We then take the spin to be

$$S \approx S_s \qquad (7)$$

and the dimensionless spin to be $\chi_s = S_s/M_s^2$. These values are reported in Table I.

A second estimate is given by comparing each spinning configuration with the irrotational one. From Table I we observe that the spin does not contribute significantly to the ADM masses. Assuming that the differences in the total angular momentum are due to the spins of the stars, we write

$$S \approx (J_{\text{ADM}} - J_{\text{ADM}}^{\text{irr}})/2. \tag{8}$$

Dimensionless spin values are given then by $\chi = S/M_s^2$. The results are stated in Table I and differ from the previous estimate by $\sim 10\%$.

A precise value of the dimensionless spin is necessary to construct binding energy vs orbital angular momentum curves. We will show that a nontrivial agreement with analytical results can be obtained using Eq. (7).

III. NUMERICAL METHOD

Simulations are performed with the BAM code [50–53]. The Einstein equations are written in $3 + 1$ BSSNOK form [54–56]. $1 + \log$ and gamma-driver conditions are employed for the evolutions of lapse and shift, respectively [57–59]; see Ref. [60] for a study of gauge condition performance in handling gravitational collapse. General relativistic hydrodynamics (GRHD) equations are solved in conservative form by defining Eulerian conservative variables from the rest-mass density ρ, pressure p, internal energy ϵ, and 3-velocity v^i. An equation of state closes the system. We consider evolutions with a Γ-law EOS

$$p = (\Gamma - 1)\rho\epsilon, \tag{9}$$

with $\Gamma = 2$ for most of the configurations. Some control runs with a polytropic EOS, thus forcing a barotropic evolution, have also been performed (see Table I.)

The evolution algorithm is based on the method of lines with explicit fourth-order Runge-Kutta time integrators. Finite differences (fourth-order stencils) are employed for the spatial derivatives of the metric. GRHD is solved by means of a high-resolution shock capturing method [50] based on primitive reconstruction and the Local-Lax-Friedrichs central scheme for the numerical fluxes. Primitive reconstruction is performed with the fifth-order WENO scheme of Ref. [61], which has been found to be important for long-term accuracy [16,17]. The numerical domain is made of a hierarchy of cell-centered nested Cartesian grids. The hierarchy consists of L levels of refinement labeled by $l = 0, \dots, L - 1$. A refinement level l has one or more Cartesian grids with constant grid spacing h_l and n points per direction. The refinement factor is 2, such that $h_l = h_0/2^l$. The grids are properly nested, in that the coordinate extent of any grid at level l, $l > 0$, is

TABLE II. Summary of the grid configurations used for the evolutions; see Sec. III for a detailed description.

Name	L	l^{mv}	n^{mv}	h_{L-1}	n	h_0
L1	6	2	128	0.225	128	7.20
L2	6	2	144	0.200	144	6.40
M	6	2	168	0.171	168	5.49
H	6	2	192	0.150	192	4.80

completely covered by the grids at level $l - 1$. Some of the mesh refinement levels $l > l^{\text{mv}}$ can be dynamically moved and adapted during the time evolution according to the technique of "moving boxes." The Berger-Oliger algorithm is employed for the time stepping [62], though only on the inner levels. Interpolation in Berger-Oliger time stepping is performed at the second order. A Courant-Friedrich-Lewy factor of 0.25 is employed in all runs. We refer the reader to Refs. [50,51] for more details.

The grid configurations considered in this work are reported in Table II. Because we evolve equal-mass binaries, we use bitant symmetry (evolving only the half-space $z > 0$) without loss of generality. We experimentally found that the nonconservative mesh refinement in BAM can lead to rest-mass violations during the postmerger phase (when mass crosses AMR boundaries), and in turn degrade the quality of the simulation in the long term. In order to minimize this systematic source of error, the number of points in the moving levels is set equal to that in the nonmoving ones; see Appendix C for more details. This is different from what was done in previous BAM simulations, that instead mostly focused on the orbital phase, e.g. Ref. [50].

Gravitational radiation is computed by means of the Weyl scalar [51] on a coordinate sphere of radius $r = 400$. The scalar is projected onto spin-weighted spherical harmonics to compute the multipoles ψ_{lm}^4. The metric multipoles h_{lm} are calculated by integrating the relation $\psi_{lm}^4 = \ddot{h}_{lm}$. We use a frequency-domain procedure with a low-frequency cutoff [63]. The signal is integrated from the very beginning of the simulation in order to include also the initial burst of radiation related to the conformal flatness of the initial data. The radiated energy and angular momentum perpendicular to the orbital plane are calculated as

$$\mathcal{E}_{\text{rad}} = \frac{1}{16\pi} \sum_{l,m}^{l_{\text{max}}} \int_0^t dt' |r\dot{h}_{lm}(t')|^2, \tag{10}$$

$$\mathcal{J}_{z\,\text{rad}} = \frac{1}{16\pi} \sum_{l,m}^{l_{\text{max}}} \int_0^t dt'\, m[r^2 h_{lm}(t')\dot{h}_{lm}^*(t')] \tag{11}$$

with $l_{\text{max}} = 8$. In the calculation of the total angular momentum $\mathcal{J}_{\text{rad}}$, we also include the $\mathcal{J}_{x,y\,\text{rad}}$ components,
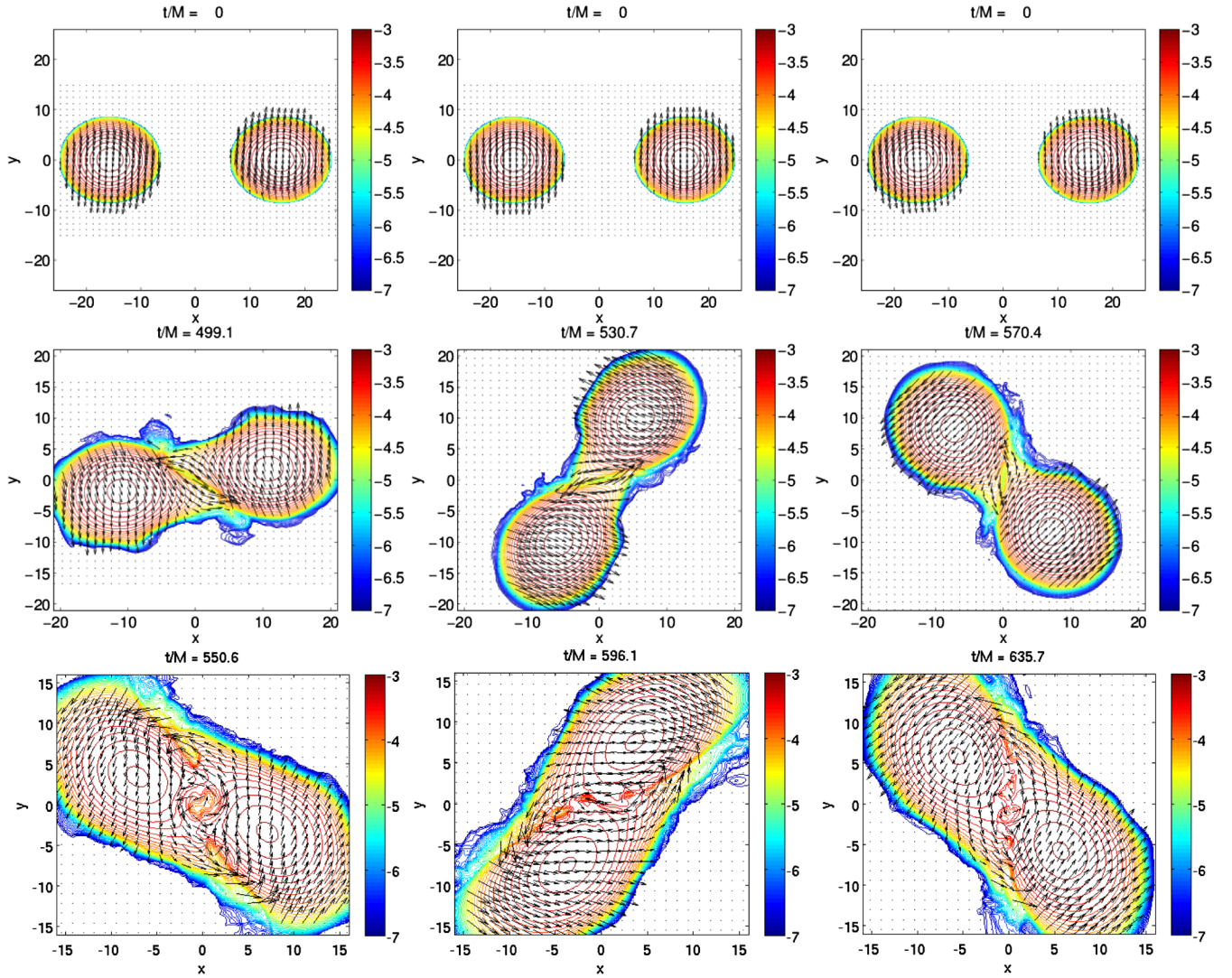
FIG. 1 (color online).   Snapshots of $\log_{10}\rho$ and (v^x, v^y) on the orbital plane. Rows from top to bottom refer to initial, contact and merger times. Columns from left to right refer to models Γ^{--}_{050}, Γ_{000} and Γ^{++}_{050}, respectively. Note the different spatial scales.

although their contribution is nonzero only in the post-merger phase and in practice negligible.

IV. DYNAMICS

In this section, we discuss the effect of the star's rotation on the binary dynamics. We formally define the merger as the peak of the amplitude $|rh_{22}|$ (Sec. V), but recall that the two stars come into contact well before (see e.g. the discussion in Ref. [16] and below). First we describe the orbital phase, i.e. evolution up to merger, and then we consider the postmerger phase.

A. Orbital motion

Figure 1 shows snapshots of the rest-mass density and fluid velocity (v^x, v^y) on the orbital plane for the representative models Γ^{--}_{050}, Γ_{000}, and Γ^{++}_{050} (columns). We focus on

these, since they are the Γ-law EOS evolutions with the highest spin magnitudes. In the plot, the stars orbit each other counterclockwise. The top row refers to the initial time; comparing the central panel (Γ_{000}) with the left (Γ^{--}_{050}) and the right (Γ^{++}_{050}), one can see only a very small difference in the velocity pattern due to the rotational state of the CRV data with respect to the irrotational flow. The central row refers to a simulation time at which the cores of the two stars come into contact; i.e. the rest-mass-density layers $\rho \sim 10^{-4}$ (10^{14} g/cm^3) of the two stars touch each other in the characteristic shearing contact, e.g. Ref. [29]. The proper distance between the stars, as calculated from the local minima of the lapse function or local maxima of ρ, is about $D \sim 30$ at this moment. Note also the very different orbital phases of the three models at this moment, revealing that the moderate initial spins had a significant effect after only about 1.5 orbits. The last row refers to the merger

time, after approximately three orbits (or 6 to 7 GW cycles; see below), at which hypermassive neutron stars (HMNSs) are formed for the three configurations. The HMNSs appear similar in the snapshots, but their angular momentum is actually different, and different dynamics follows (see Sec. IV B).

The orbital dynamics of the irrotational model is consistent with what was previously observed in e.g. Ref. [50] for the same initial configuration computed with the Lorene code (see also Appendix C). The star rotation changes this picture: for spins aligned with the orbital angular momentum, the inspiral is longer for larger spin magnitudes, while for antialigned spins, the inspiral is shorter for larger spin magnitudes. This effect can be understood in term of spin-orbit interaction [64]. Analogously to what happens to corotating/counterrotating circular orbits in Kerr spacetimes, the last stable spherical orbit moves outwards (inwards) for antialigned (aligned) spin configurations with respect to the nonspinning case [64]. The analogous result in binary black hole simulations is sometimes called "hang-up" [65]. In BNS mergers it has been discussed recently in Refs. [41,42]. Spin-orbit interactions thus change quantitatively the binary dynamics, and we quantify this aspect in the following.

A gauge-invariant way to analyze the binary dynamics from numerical relativity data is to consider binding energy vs orbital angular momentum curves, as proposed in Ref. [38]. In the present context, these curves allow us to characterize the dynamics generated by CRV initial data. We compute the dimensionless binding energy and angular momentum per reduced mass as[1]

$$E = [(M_{\mathrm{ADM}}(t=0) - \mathcal{E}_{\mathrm{rad}})/M - 1]\nu^{-1}, \quad (12)$$

$$\ell = (L - \mathcal{J}_{\mathrm{rad}})(M^2\nu)^{-1}, \quad (13)$$

respectively, where $\nu = 1/4$ is the symmetric mass ratio and the isolation mass M is taken as $M = 2M_s$; see Table I. The initial angular momentum L is computed from the spin estimates of Sec. II C as

$$L = J_{\mathrm{ADM}}(t=0) - 2S_s \quad (14)$$

and coincides with $J_{\mathrm{ADM}}(t=0)$ for the irrotational configuration. Equation (13) assumes that $\mathcal{J}_{\mathrm{rad}}$ only affects ℓ; i.e. the spin magnitude remains constant. This can be justified on a PN basis, and in general, it holds for small, aligned spins.

The numerical data $E(\ell)$ are compared to *point-mass* analytical results: a post-Newtonian (PN) and an effective one-body (EOB) [66,67] curve. In this work, we employ

---

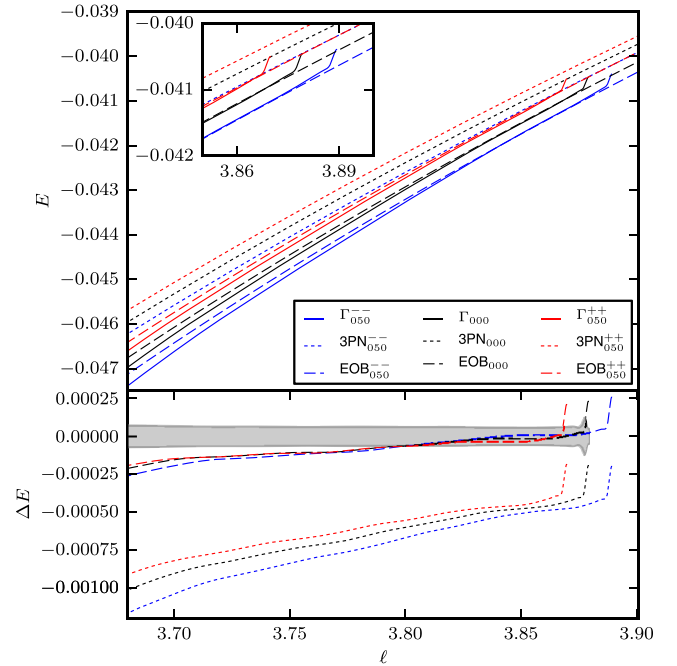[1]The notation for the angular momentum is slightly different from that of Ref. [38].

FIG. 2 (color online). Binding energy vs orbital angular momentum curves for models Γ_{050}^{--}, Γ_{050}^{++} and Γ_{000}. Top: $E(\ell)$ curves for numerical data (solid lines), 3 PN (dotted lines), and EOB (dashed lines). Bottom: Differences $\Delta E = E - E^X$ between numerical data and 3 PN (dotted) and EOB curves (dashed). The uncertainty on the numerical data is shown in light gray.

the 3 PN binding energy expression, including next-to-next-to-leading-order spin-orbit coupling as given by Eq. (43) of Ref. [68], and indicate it as $E^{3\mathrm{PN}}(\ell)$. The results rely on earlier achievements in PN theory, among others; see Refs. [69–75]. Additionally, we also consider the curve $E^{\mathrm{EOB}}(\ell)$ constructed within the EOB approach in the adiabatic limit. For simplicity, we use the EOB model for spinning binaries introduced in Ref. [64]. Similarly, the nonspinning part of the model is taken at 3 PN accuracy [76] only, and it is resummed with a (1,3) Padé approximant (see Refs. [77–80] for recent theoretical developments of the EOB model). The next-to-leading-order [81] and next-next-to-leading-order [68] spin-orbit couplings are included in the Hamiltonian. We restrict ourselves to the leading-order spin-spin term for simplicity, although the spin-spin interaction is known at next-to-leading order [82].

There is evidence that irrotational, conformally flat initial data sequences are quite close to the 3 PN result for a sufficiently large binary separation, e.g. Ref. [27] (and also Appendix B). However, we recall that the conformally flat approximation introduces errors already at the 2 PN level [76]. On the other hand, the 3 PN-EOB adiabatic curve has been found to correctly reproduce nonspinning numerical relativity data of different mass ratios up to $\ell \sim 3.55$ [38]. The same reference has shown that the
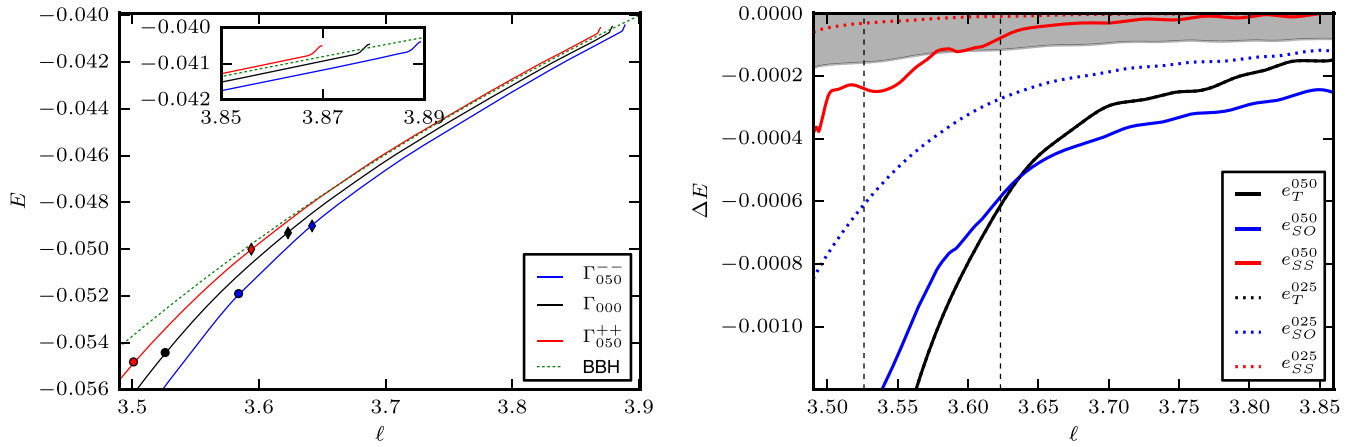
FIG. 3 (color online).   Binding energy vs orbital angular momentum curves for Γ models and a nonspinning BBH run. Left: $E(\ell)$ curves for BNS and BBH data. Diamonds and bullets indicate the approximate moment of contact (corresponding to the snapshots of Fig. 1) and the moment of merger, respectively. Right: Different contributions to the binding energy in Eq. (15), extracted from differences of data sets as described in the text. The uncertainty of the numerical data is shown as the gray shaded region. The vertical dashed lines refer to the approximate moment of contact and to the merger for Γ_{000}. e_T^{025} and e_T^{050} coincide in this plot. Doubling the spin approximately doubles the spin-orbit effect in the binding energy. For 0.05, the spin-orbit term is larger than the tidal term until $\ell \sim 3.65$.

3 PN-EOB curve is instead remarkably close to numerical data up to the last stable orbit of the EOB potential ($\ell \sim 3.28$), and it is an accurate diagnostic of the *conservative dynamics* of the system. (See Ref. [17] for the case of neutron star mergers with irrotational data.)

The curves $E(\ell)$ at early simulation times are shown in Fig. 2 for the models Γ_{050}^{--}, Γ_{000}, and Γ_{050}^{++}, together with the PN and EOB curves computed with the spin values as estimated in Sec. II C. These curves are quite sensitive to small variations in the values of the initial masses, angular momentum and spins. For example, they require M_{ADM} and M_s to be accurate up to four digits. The uncertainty on the numerical data is also shown. It is estimated by considering Γ_{000} data at different resolutions (grid configurations H and L2) and including the uncertainty of the initial ADM values as measured from different SGRID resolutions. Both errors are added in quadrature. The bottom panel shows the differences $\Delta E = E - E^X$ of numerical data with respect to the $X = $ 3PN and the $X = $ EOB curves with the relative spin values.

We experimentally observe that, for all the configurations considered in this work, the spin estimate in Eq. (7) leads to $E(\ell)$ curves closer than those estimated by Eq. (8) to the PN and EOB ones at early times. Thus, we use that estimate in the figure and in the following. Note that this choice assumes that the spin is almost constant along the sequences.

As shown in Fig. 2, the dynamics starts between the PN and EOB curves and rapidly departs from the initial state, $\ell \sim 3.87$ (see inset). This variation is due to the emission of the artificial gravitational radiation related to the conformally flat assumption of the CRV data. In complete analogy with the nonspinning binary black hole case and the

irrotational case, the numerical evolution settles very quickly close to the EOB curve (with the proper spin) [17,38]. The difference between the EOB curves and the numerical data at early times is within the error bars: the tidal contribution cannot be distinguished with present data (the same happens comparing BNS and BBH; see below).

A clear hierarchy among the PN and EOB curves with different spins can be observed. This effect is due to spin-orbit interactions: antialigned configurations are more bound and aligned configurations are less bound than irrotational (cf. "hang-up"). The numerical curves consistently respect such hierarchy from early times to merger (see below). During the early-time evolution, the binaries' binding energies depart systematically from the EOB, and close to contact ($\ell_c \sim 3.63$), the deviation becomes significant. Note in the bottom panel how the differences between the EOB and numerical data for different spins are essentially indistinguishable. This fact clearly suggests that the deviation is due to finite size effects.

The curves $E(\ell)$ up to merger are shown in Fig. 3 (left panel) for the models Γ_{050}^{--}, Γ_{000}, and Γ_{050}^{++} together with the one for the nonspinning BBH run. At early times (see inset), the BBH system is less bound than the irrotational configuration, but within the data uncertainty. As observed for the EOB curve, for $\ell \to \ell_c$ tidal contributions become progressively more important, and the systems become more bound, deviating systematically from the BBH curve. Merger occurs at $\ell_m \sim 3.58$, 3.53, 3.50 for Γ_{050}^{--}, Γ_{000} and Γ_{050}^{++}, respectively. At merger, the aligned spin configurations are more bound than the antialigned one. See also Table III for a collection of relevant numbers for all the configurations.

TABLE III. Dynamical quantities during orbital motion. Simulation time, gravitational wave frequency, angular momentum, and energy are reported at the moments of contact and merger. Note that the contact time is not a well-defined quantity and is just reported to give a rough estimate. Frequencies have uncertainties of about 10%.

Name	t_c/M	$M\omega_c$	ℓ_c	$E_c \times 10^2$	t_m/M	$M\omega_m$	ℓ_m	$E_m \times 10^2$
Γ_{050}^{--}	499	0.067	3.64	−4.89	551	0.124	3.58	−5.19
Γ_{025}^{--}	514	0.065	3.63	−4.90	575	0.128	3.55	−5.36
Γ_{000}	531	0.069	3.62	−4.92	595	0.127	3.53	−5.44
Γ_{025}^{++}	549	0.070	3.61	−4.95	618	0.125	3.51	−5.47
Γ_{050}^{++}	570	0.071	3.60	−4.99	636	0.123	3.50	−5.48

In order to gain insight into the role of spin and tidal interactions during the merger phase, we make the assumption that

$$E \approx e_0 + e_{\rm SO} + e_{\rm SS} + e_T; \qquad (15)$$

i.e. that the binding energy of a spinning BNS configuration can be approximated by the *sum* of four separate contributions: a nonspinning point-mass (black-hole) term e_0, a spin-orbit (SO) term $e_{\rm SO}$, a spin-spin (SS) term $e_{\rm SS}$, and a tidal (T) term e_T. The different terms have PN contributions starting from 1.5 PN (SO), 2 PN (SS), and 5 PN (T). All four terms in Eq. (15) can be calculated using the simulation data, e.g. the four runs Γ_{000}, Γ_{050}^{++}, Γ_{050}^{--}, and BBH. Below we distinguish between the terms in the ansatz (e_x) and the numerical curves (E_X^Y, as the relative model name). The SO term has structure of the form $\propto \mathbf{L} \cdot \mathbf{S}$, so for aligned/antialigned spins, $e_{\rm SO} \propto 2\text{sign}(S)|\mathbf{L}||\mathbf{S}|$. Similarly, the SS term has structure $\propto \mathbf{S}_1 \cdot \mathbf{S}_2$, so it does not change sign if both spins flip. A ++ binary configuration has a repulsive SO contribution ($e_{\rm SO} > 0$), whereas a −− one with the same spin magnitude has an attractive SO contribution ($e_{\rm SO} < 0$) to the binding energy. However, as mentioned above, the aligned spin configurations give a more negative binding energy at merger than the anti-aligned configurations (compare with Ref. [64]).

The SO term is calculated by the combination of the aligned/antialigned spin runs with the same magnitude, i.e. $e_{\rm SO} \approx (E_{050}^{++} - E_{050}^{--})/2$. Obviously, we pose $e_0 \approx E_{\rm BBH}$ and $e_0 + e_T \approx E_{000}$, and we calculate e_T from the difference $E_{000} - E_{\rm BBH}$. The SS term is estimated as $e_{\rm SS} \approx (E_{050}^{++} + E_{050}^{--})/2 - E_{000}$. The different terms e_x are reported in the right panel of Fig. 3. The SS contribution is the smallest negative, at the level of the uncertainty of the data. At the moderate spins used here, SS interactions are essentially not resolved in the simulation. On the other hand, the curves $e_{\rm SO}$ and e_T are well resolved. We observe that, for $\chi = 0.05$, the $e_{\rm SO}$ is the dominant contribution to the binding energy up to $\ell \sim 3.65$. After this point, e_T becomes dominant. This corresponds to intuition, since the dynamics reaches the hydrodynamical regime (see Fig. 1). Towards merger (not visible in the plot), the differences between the $e_{\rm SO}$ and e_T become progressively larger.

An independent estimate of $e_{\rm SO}$, e_T, and $e_{\rm SS}$ is also given by using the data of the other two simulations Γ_{025}; see the right panel of Fig. 3. We obtain similar results, and in particular the e_T terms exactly coincide as they should. There is one important difference, though. In the case $\chi = 0.025$, the e_T term is the largest negative term already at early simulation times. Thus, during the last three orbits the binding energy is "tidally dominated" as in the irrotational case.

We mention that, while the SS term is poorly resolved, its presence is clearly suggested by looking at the difference $E_{000} - E_{050}^{++}$ and $E_{050}^{--} - E_{000}$. The two combinations approximate $e_{\rm SO} \pm e_{\rm SS}$, with the SS term entering with a different sign. We find that, as expected, the former is less bound; the latter is more so by a small amount. Similarly, inspection of the quantity $(E_{050}^{++} - E_{050}^{--})/2 - E_{\rm BBH} \approx e_T + e_{\rm SS}$ leads to a curve very close to e_T, only slightly more bound. This suggests that there is no significant coupling between SO and tidal contributions [as assumed in Eq. (15)], even after contact.

Finally, note that for $\ell \lesssim \ell_c$, the spin term $e_{\rm SO} + e_{\rm SS}$ is probably influenced by hydrodynamical effects, so its correct interpretation may be nontrivial. We also mention that similar results and conclusions are obtained by using the EOB curves instead of the BBH data.

B. Merger remnant

All the configurations evolved with the Γ-law EOS form, at merger, HMNSs characterized by different rotational states. In our simulations, the HMNS is only supported by centrifugal forces and thermal pressure (we include neither magnetic fields nor cooling mechanisms). The angular momentum support is radiated away in GWs on dynamical time scales, and the HMNS finally collapses. This happens after about 1500 M ($\sim$22 ms) from formation in the irrotational model. The dimensionless angular momentum magnitude per reduced mass of the HMNS is approximately $j \approx \ell_m \pm 2\chi/\nu$ (assuming $\chi \sim$ const.), e.g. $j \sim 3.18$, 3.53, 3.9 for Γ_{050}^{--}, Γ_{000}, and Γ_{050}^{++}, respectively. We thus expect that configurations with antialigned spins will collapse earlier, whereas configurations with aligned spins will collapse later.

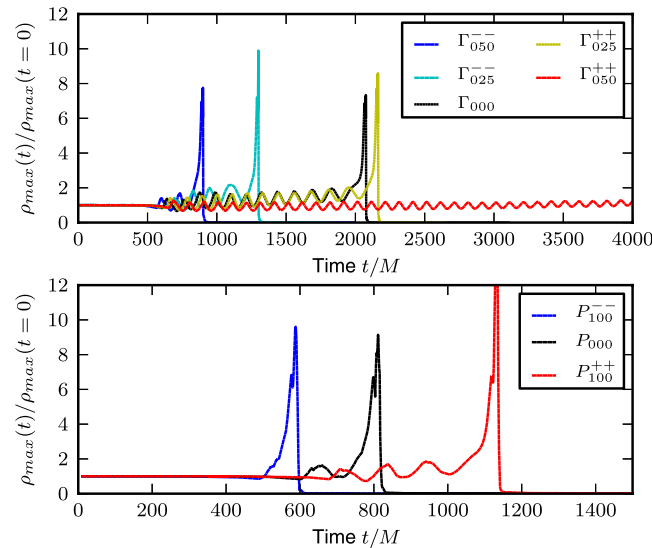In Fig. 4 we show the evolution of the maximum rest-mass density, $\rho_{\rm max}(t)$, for evolutions with the Γ-law EOS

FIG. 4 (color online). Evolution of the maximum mass-density $\rho(t)$ (normalized by its initial value) for the configurations Γ_{050}^{++}, Γ_{025}^{++}, Γ_{000}, Γ_{025}^{--} and Γ_{050}^{--} (upper panel) and for the configurations P_{100}^{++}, P_{000} and P_{100}^{--} (lower panel). Note the different x axes.

FIG. 5 (color online). Evolution of projections $\rho_m(t)$ for $m = 1$, 2, 3, 4 and different models. From top to bottom: Γ_{050}^{--}, Γ_{000}, Γ_{050}^{++}.

(upper panel) and the polytropic EOS (lower panel). The oscillations visible in the plot correspond to quasiradial modes (see below and Sec. V). The average rest-mass density increases linearly in time to about a critical density, $\rho_c \sim 2\rho_{\max}(t = 0)$ ($\rho_c \sim 1.2 \times 10^{15}$ g/cm³), at which collapse happens. As expected, we observe that model Γ_{050}^{--} collapses after approximately 2 quasiradial oscillations, model Γ_{025}^{--} after 5, and model Γ_{025}^{++} after 12. Model Γ_{050}^{++} survives for several dynamical timescales and does not collapse until the end of the simulation ($t \sim 4000$ M). We have not evolved Γ_{050}^{++} further, since (i) long-term simulations can become inaccurate (see Appendix C), and (ii) on these timescales other physical effects like magnetic fields and neutrino cooling, presently not included, play an important role, e.g. Refs. [30,83–85]. However, considering a linear trend in $\rho_{\max}(t)$, we extrapolate that collapse should happen at about ~167000 M (~272 ms) after merger.

The lower panel of Fig. 4 refers to configurations evolved with a polytropic EOS. Since in this case thermal pressure support is absent, collapse occurs much earlier than for the Γ-law EOS. The HMNS of the irrotational configuration collapses after about 1 quasiradial oscillation; model P_{100}^{--} promptly collapses without HMNS formation, and model P_{100}^{++} collapses after a few oscillations.

During its evolution, the HMNS oscillates nonlinearly and becomes progressively more compact. The oscillation modes can be identified as the quasiradial mode, the $m = 2$ f mode, and nonlinear combinations of them, e.g. Refs. [39,86]. A way to characterize nonlinear modes is to project the rest-mass density onto spherical harmonics,
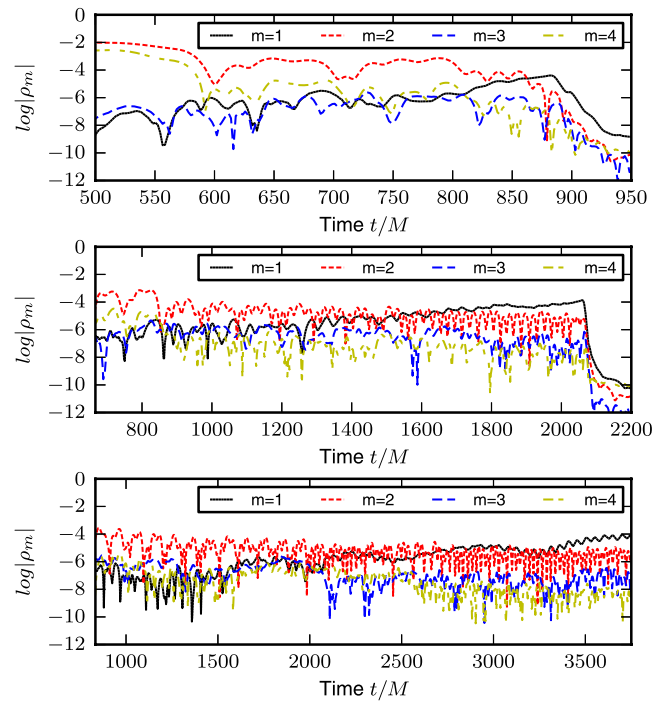
e.g. Ref. [87]. For simplicity, we consider $\rho(x, y, z = 0, t)$ in the orbital plane $z = 0$ and the projections [86]

$$\rho_m(t) = \int \rho(x, y, z = 0, t)e^{im\phi(x,y)}\mathrm{d}x\mathrm{d}y. \quad (16)$$

In Fig. 5 we report the evolution of the first projections $m = 1$, 2, 3, 4 for some representative runs. The figure shows that the dominant mode is the $m = 2$ mode. Actually, the projection/mode with larger amplitude is the quasiradial one ($m = 0$, also visible in $\rho_{\max}$ Fig. 4). As we shall discuss later, however, this mode has a frequency too low to be visible in the GW spectrum. The evolution of $\rho_m(t)$ is qualitatively similar in the different configurations, with differences only related to the collapse time. A strong $m = 1$ mode appears in *all* simulations before collapse (see e.g. the central panel) and also dominates the evolution of Γ_{050}^{++} after $t \sim 3500$ M. We interpret it as a physical hydrodynamical effect due to mode couplings, but we cannot rule out that it is triggered by some numerical effect.

In order to extract the mode frequencies, we perform a Fourier analysis of the ρ_m projections and $\rho_{\max}$. The quasiradial mode is best extracted from the latter. The Fourier transform is performed only in the part of the signal after merger, i.e. $t > t_m$. Some of the relevant results are summarized in Fig. 6, where we show on the left the spectra of $\rho_{\max}$ for lower frequencies and ρ_2 for higher frequencies for different models and on the right the spectrogram of model Γ_{050}^{++}. Focusing on the left panel, we observe that the
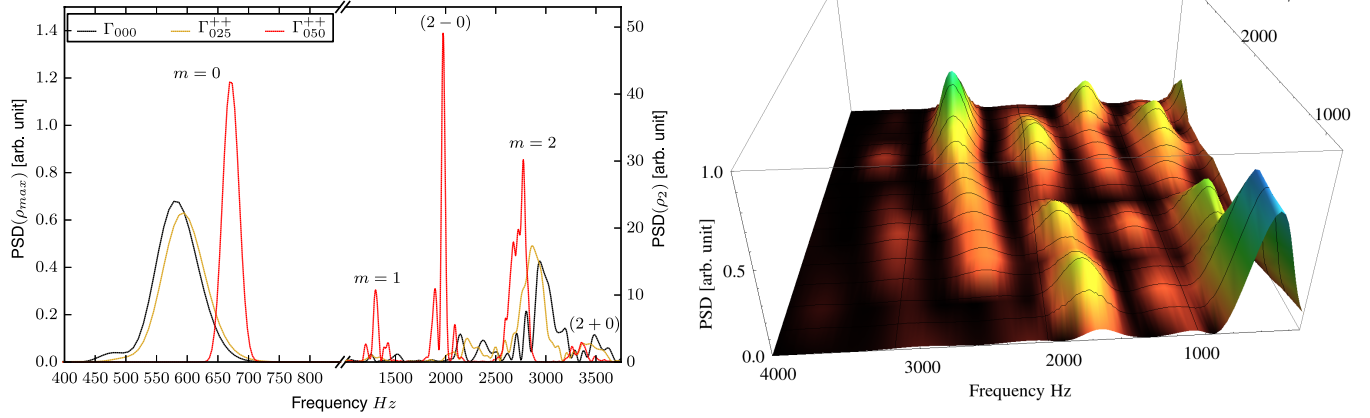
FIG. 6 (color online). Fourier analysis of the rest-mass projections ρ_m. Left: Power spectral density (PSD) of $\rho_{\max}(t)$ and $\rho_2(t)$ for Γ_{000}, Γ_{025}^{++}, Γ_{050}^{++}. Right: Spectrogram of the quantity $\rho_{12}(t) \equiv \rho_1(t) + \rho_2(t)$ in model Γ_{050}^{++}.

spectrum is composed of few frequencies; we identify $m = 0, 1, 2$ modes together with nonlinear couplings "2 ± 0" [86–88]. For model Γ_{050}^{++}, the highest power is actually found at the "$2 - 0$" frequency in ρ_2.

The peak frequencies for the different modes and models are stated in Table IV for the relevant case of spin aligned with the orbital angular momentum. The frequency peak of the $m = 2$ mode becomes larger the smaller the HMNS rotation is. This is because the HMNS with more angular momentum support is less compact, and the proper frequencies decrease if the compactness decreases (compare with sequences of a single rotating star with the same rest mass in Ref. [88]). Notably, for model Γ_{050}^{++}, the observed frequency shift with respect to the irrotational configuration is 236 Hz. The value is significant at the 1σ level; see Table IV. Differently from the $m = 2$ mode, the frequency of the quasiradial mode ($m = 0$) is found to increase for HMNSs with larger angular momentum. As discussed in Ref. [86], the quasiradial mode frequency depends on the compactness of the HMNS and on how close the star model is to the collapse-instability threshold. The larger the compactness, the larger the mode frequency is, but configurations close to the instability threshold can have smaller frequencies, since the instability threshold is a neutral point. We interpret our results according to the above argument: HMNSs with larger angular momentum support are further from the collapse threshold and thus have higher frequencies.

The spectra lines appear broad due to the highly dynamical nature of the HMNS. Investigating the dynamical excitation of the modes by a spectrogram, we find that (i) the modes are "instantaneously" characterized by relatively narrow peaks; (ii) different modes dominate different parts of the signal; and (iii) some of the peaks "drift" towards higher frequencies as the HMNS becomes more compact. The right panel of Fig. 6 shows the spectrogram of the quantity $\rho_{12}(t) \equiv \rho_1(t) + \rho_2(t)$ for

Γ_{050}^{++}. At early times, the $m = 0$ (quasiradial) mode dominates the ρ_{12} spectrum, but around $t \sim 2000$ M, the $m = 2$ becomes the main oscillation mode. A "drift" of the $m = 2$ mode towards higher frequencies is visible, which corresponds to the fact that the HMNS becomes more compact. The "$2 - 0$" coupling remains the secondary peak during the whole simulation. The $m = 3$ and "$2 + 0$" modes are also visible. At the very end of the evolution, the $m = 1$ mode has the largest power.

Finally, we briefly discuss the black hole and the remnant disk. All simulations (except Γ_{050}^{++}) result in a black hole surrounded by a nonmassive accretion disk. Table V summarizes the irreducible mass and the dimensionless spin of the black hole, and the rest mass of the disk. The black hole mass is larger for antialigned spin configurations and spin magnitude, and a monotonic trend is observed for smaller spin and aligned spin configurations. The opposite holds for the disk mass. The spin of the black hole is larger for aligned configurations in barotropic evolutions. This effect is not visible in the Γ-law simulations, in which the more massive disk probably also has larger angular momentum. The maximum spin produced is 0.84, which is consistent with the upper limit found in Ref. [41]. Notice that all reported quantities are affected by large uncertainties, and they should be considered only as a qualitative indication. For example, the uncertainty on the black hole mass calculated from L_2 and H runs of the irrotational configuration is ~ 0.01.

V. GRAVITATIONAL RADIATION

The dynamics described in Sec. IV is relatively simple (but far from trivial). For sufficiently high spin magnitudes, $\chi \sim 0.05$, the SO interaction is a significant repulsive (attractive) contribution for aligned (antialigned) spin configurations. For aligned configuration, the SO competes with finite size effects. At merger, however, binaries with

TABLE IV. Peak frequencies of the power spectral density (PSD) of ρ_m and ρ_{max}. They are estimated by fitting a Gaussian of standard deviation σ. The value of the latter is reported in parenthesis.

	$m = 0$	$m = 1$	$m = 2$
Γ_{000}	584 (34)	1543 (38)	2974 (114)
Γ_{025}^{++}	594 (34)	1482 (38)	2871 (103)
Γ_{050}^{++}	671 (13)	1341 (13)	2738 (76)

TABLE V. Important quantities for the merger remnant. Stated are the black hole mass, the dimensionless spin of the black hole, and the absolute disk mass of the surrounding disk, as well as the percentage with respect to the total baryonic mass.

	Γ_{050}^{--}	Γ_{025}^{--}	Γ_{000}	Γ_{025}^{++}	P_{100}^{--}	P_{000}	P_{100}^{++}
M_{BH}	2.92	2.88	2.85	2.86	2.95	2.94	2.89
χ_{BH}	0.80	0.79	0.78	0.79	0.81	0.83	0.84
$M_{b,disk}$	0.039	0.068	0.081	0.082	0.006	0.021	0.065
$M_{b,disk}/M_b$	1.2%	2.1%	2.5%	2.5%	0.2%	0.6%	2.0%

aligned spins are more bound. HMNSs are formed with more or less angular momentum support than in the irrotational configuration ($j \sim \ell_m \pm 2\chi/\nu$); thus, they are either closer to or farther from the collapse threshold (radial instability point). We discuss in this section how the emitted gravitational radiation encodes all this.

The total energy and angular momentum emitted in GWs quite differ in the different models, as can be seen from Fig. 7. The irrotational configuration emits about 1.2% of the initial ADM mass and 18% of the initial angular momentum. Γ_{050}^{--} emits about the same amount, but in about half the time. To the end of the simulation, Γ_{050}^{++} has emitted 0.8% of the initial mass and about 15% of the initial angular momentum. In all the cases, the main emission channel is the $l = m = 2$ multipole that alone accounts for $\sim$97% of the emitted energy. However, in the postmerger phase other channels are clearly excited; the largest amplitudes are observed in the $l = 2$, $m = 0$; the $l = 3$, $m = 3, 2$; and the $l = m = 4$ modes (in that order).

Figure 8 (left panel) shows the $l = m = 2$ inspiral waveforms, focusing again on the models Γ_{050}^{--}, Γ_{000} and Γ_{050}^{++} for clarity. Intermediate results are, of course, found for the other models. The upper-left panel shows the real part and amplitude of the $l = m = 2$ mode of the GWs, and the lower-left panel shows the GW frequency $M\omega_{22} = -\Im(\dot{h}_{22}/h_{22})$; note the retarded time in the x axis. The merger times, computed at the peak of $|rh_{22}|$, are $t_m \sim 595$, 551, and 636M for Γ_{000}, Γ_{050}^{--} and Γ_{050}^{++}, respectively (see also Table III). The peaks of the wave amplitude are all very close to $\sim$0.7. The GW frequency corresponding to the peak of the wave amplitude is smallest for aligned spin. At merger, $M\omega_{22} \sim 0.127$, 0.124, and 0.123 for Γ_{000}, Γ_{050}^{--}, and Γ_{050}^{++}, respectively. At contact, instead, $M\omega_{22} \sim 0.069$,
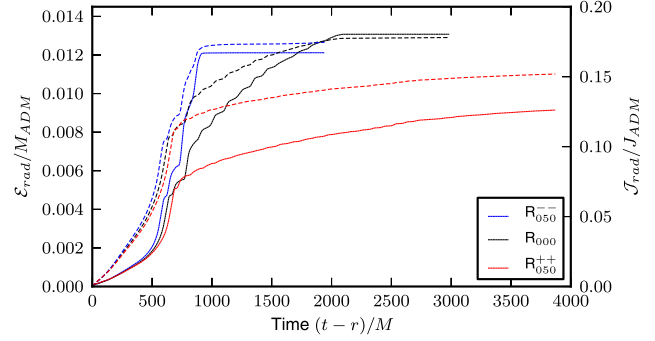

FIG. 7 (color online). Energy (solid lines) and angular momentum (dashed lines) radiated in GWs for models Γ_{050}^{--}, Γ_{000}, and Γ_{050}^{++}.

0.067, 0.071. Note that these frequencies have uncertainties of about 10%. The effect of spin-orbit interaction is clearly visible from the plot. Computing the accumulated phase of the GW, we find that the irrotational configuration emits 7.0 GW cycles to merger; Γ_{050}^{--} emits 6.3 cycles and Γ_{050}^{++} emits 7.3 cycles. This phase difference results from the dynamics discussed in Sec. IV A and encodes the interplay of spins and tidal interactions.

Let us finally discuss the emission from the HMNS. Figure 8 (right panel) shows the $l = m = 2$ complete waveform. The earlier the HMNS collapses, the larger the amplitude of the wave in the postmerger phase is. As also shown in Fig. 7, model Γ_{050}^{--} emits more energy and angular momentum than Γ_{000} and Γ_{050}^{++} during the first $\sim$600 M after merger. In order to identify the origin of the emission, we perform a Fourier analysis of the $l = m = 2$ and $l = 2$ $m = 0$ multipoles and compare this with the mode analysis of Sec. IV B. As in the previous section, we consider only the signal at $t > t_m$. A relevant example of this analysis is summarized in Fig. 9. The spectra of the waves and matter modes strongly correlate: the HMNS modes are the main emitters during the postmerger phase [86]. We stress that the complete GW spectrum includes also the inspiral part of the GW signal. In particular, the merger happens at GW frequencies of $\sim$1.2 − 1.3 kHz, and up to these frequencies, the spectrum is dominated by the inspiral. Thus, the quasiradial mode frequency of the HMNS is not observable, whereas the $m = 2$ and "2 ± 0" peaks form the main postmerger signal.

In Refs. [40,89] (see also Ref. [84]), it is shown that the frequency of the peak of the GW (postmerger) spectrum is strongly dependent on the EOS, and to a lesser extent, on the total mass, mass ratio, and spin. The latter aspect has been investigated by comparing irrotational and corotational configurations for a few models, and no significant frequency shift was observed. The long wave train of model Γ_{050}^{++} allows us to resolve a significant frequency shift, suggesting that spin effects may be more important than previously thought. Note that a shift towards *lower* frequencies can favor GW detection by advanced interferometers.
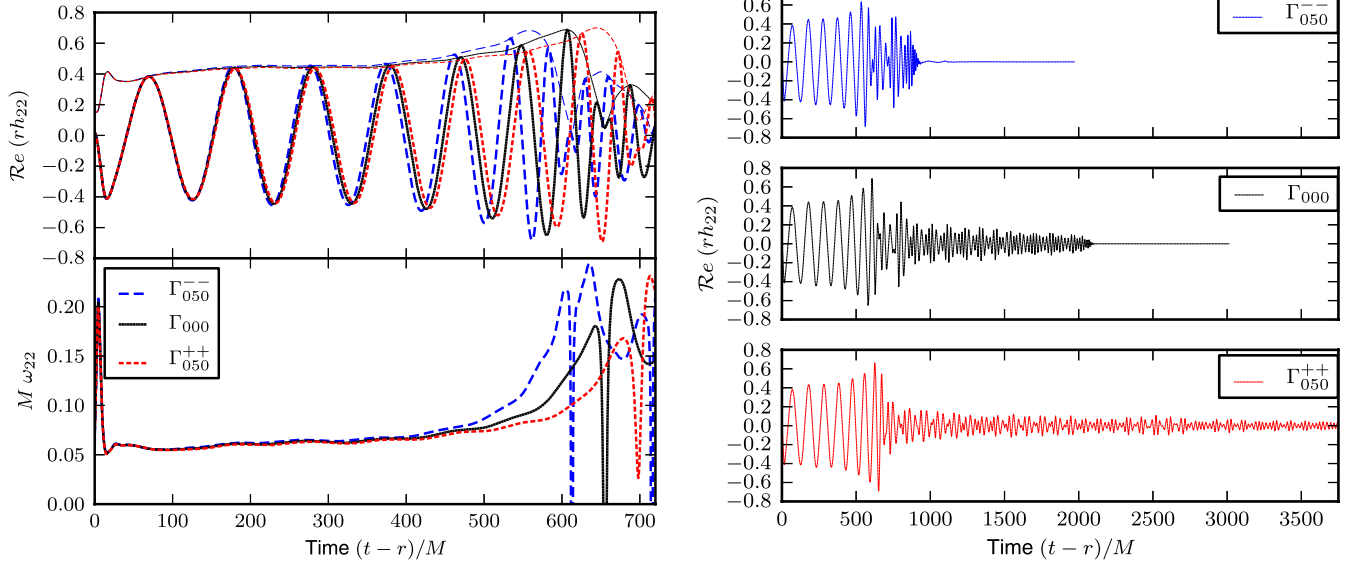
FIG. 8 (color online). Gravitational wave signal for models Γ_{050}^{--}, Γ_{000}, and Γ_{050}^{++}. Left: Inspiral waveforms $\Re(rh_{22})$ and $r|h_{22}|$, and frequency $M\omega_{22}$. Right: Full signal $\Re(rh_{22})$.
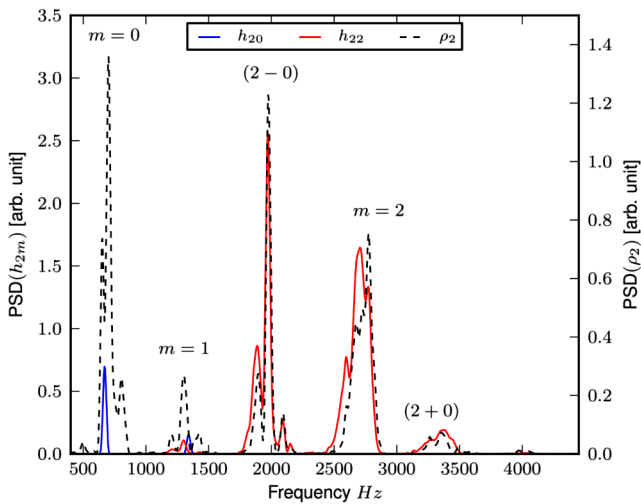

FIG. 9 (color online). Fourier analysis of the $l = 2$ postmerger waveform multipoles and matter projection ρ_2 for model Γ_{050}^{++}. The waveform frequencies strongly correlate with the fluid's modes.

VI. CONCLUSION

We have studied BNS mergers in numerical relativity with a realistic prescription for the spin. Consistent initial data have been produced with the CRV approach and evolved for the first time.

We have considered moderate star rotations corresponding to dimensionless spin magnitudes of $\chi = 0.025$, 0.05, and direction-aligned or antialigned with the orbital angular momentum. The dimensionless spins χ are estimated by considering the angular momentum and masses of stars in isolation with the same rotational state as in the binary. We

have investigated the orbital dynamics of the system by means of gauge-invariant $E(\ell)$ curves [38].

Our simple proposal for the estimation of χ proved to be robust and allows us to show consistency with PN and EOB energy curves at early times. Using energy curves, we have also compared, for the first time to our knowledge, BNS and BBH dynamics (see Ref. [90] for a waveform-based comparison of the case BBH–mixed binary). We extracted and isolated different contributions to the binding energy, namely the point-mass nonspinning leading term, the spin-orbit and spin-spin terms, and the tidal term. The analysis indicates that the spin-orbit contribution to the binding energy dominates over tidal contributions up to contact (GW frequencies $M\omega_{22} \sim 0.07$) for $\chi \sim 0.05$. The spin-spin term, on the other hand, is so small that it is not well resolved in the simulations. No significant couplings between tidal and spin-orbit terms are found, even at a stage in which the simulation is in the hydrodynamical regime (at this point, however, the interpretation of "spin-orbit" probably breaks down).

The spin-orbit interactions significantly change the GW signal emitted. During the three-orbit evolution, we observe accumulated phase differences up to 0.7 GW cycles (over three orbits) between the irrotational configuration and the spinning ones ($\chi = 0.05$)—that is, we obtain first quantitative results for orbital "hang-up" and "speed-up" effects. A precise modeling of the late-inspiral-merger waveforms, as in Ref. [17], needs to include spin effects even for moderate magnitudes. Long-term (several orbits) simulations are planned for a thorough investigation of this aspect, together with detailed waveform phasing analysis and comparison with analytical models. Extensive simulations with different EOSs will also be important to check the universal relations recently proposed in Ref. [91].

We have also investigated spin effects on the formation and collapse of the merger remnants (HMNSs) and the hydrodynamical evolution of the HMNS modes [86]. The star rotation influences the HMNS produced at merger by augmenting (aligned spin configuration) or reducing (antialigned) the angular momentum support. Earlier or delayed collapse of several milliseconds is thus observed depending on the spin's orientation. We have found that characteristic frequencies of the HMNS are shifted to *lower* values by rotation. This suggests that spin effects may be more important than previously thought. HMNS modes are the main emitters of GWs in the postmerger phase, and they may allow for a precise determination of the neutron star radius in a GW detection [89]. Extensive evolutions of CRV configurations for various EOSs and spins are needed in order to assess the role of spin and to obtain accurate phenomenological relations for frequency vs radius.

Future work should also be devoted to understanding the impact of our result on GW astronomy. We expect that some aspects of spin in BNS can be modeled similarly to the GW analysis for nonprecessing spinning BBHs [92–95]. Furthermore, it would be important to explore the relevance of spin-orbit corrections in the construction of templates for detecting the star's EOS [5,96], possibly applying realistic data analysis settings [14]. In the relevant case of aligned spin configurations, spin-orbit effects actually compete with finite size effects. One might expect that, for some realistic spin magnitudes, this could affect the measurability of the EOS (tidal polarizability parameters) when spin is not properly taken into account. Similarly, if the spin is estimated from the early inspiral, a bias in the spin magnitude could significantly affect the measure of the tidal parameters [5].

ACKNOWLEDGMENTS

APPENDIX A: SINGLE SPINNING STARS

In the CRV approach, one assumes the existence of an approximate helical Killing vector. In an inertial frame it has the form [35]

$$\xi^\mu = (1, -\Omega[x^2 - x_{CM}^2], \Omega[x^1 - x_{CM}^1], 0). \quad (A1)$$
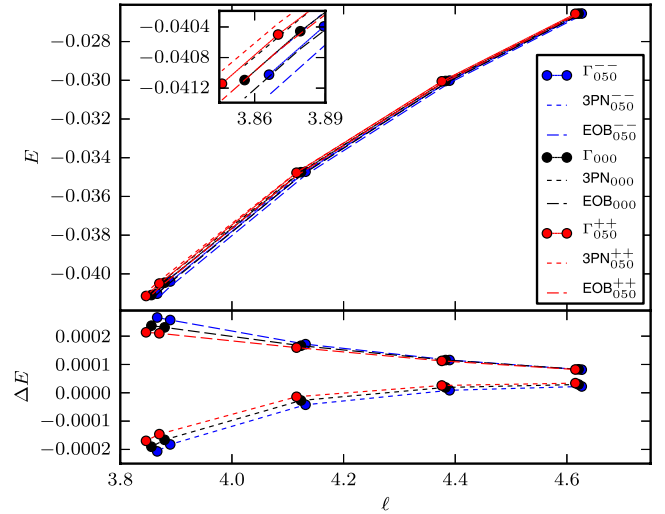

FIG. 10 (color online).   Top: Binding energy vs orbital angular momentum curves for equilibrium configurations, together with 3 PN and EOB results. Bottom: The differences $\Delta E = E - E^X$ with $X = 3$ PN, EOB (lower panel).

Here x_{CM}^i denotes the center-of-mass position of the system, and Ω is the orbital angular velocity, which we have chosen to lie along the x^3 direction.

For a single star, x_{CM}^i coincides with the star center x_{C*}^i. Furthermore, if we follow the CRV approach, $\Omega = 0$, since a single star is not orbiting. Thus, the approximate Killing vector simply points along the time direction. We can then set the ω^j in Eq. (6) to the same value as in the case of binary stars. If we now solve the CRV equations, we obtain initial data for a single spinning star. This spin can be unambiguously computed from the ADM angular momentum and reported in the S_s column of Table I.

However, there is at least one other way to obtain single spinning stars. We can set Ω to a nonzero value and assume that the approximate Killing vector is truly helical. If we then assume that the fluid velocity is along the Killing vector

$$u^\mu = u^0 \xi^\mu, \quad (A2)$$

we obtain the standard assumptions for a corotating configuration, but for a single star only. If we now solve the usual equations for the corotating case (see e.g. Ref. [47]), we also obtain initial data for a single spinning star. Notice, however, that the star spin in this corotating approach is about 10% higher than in the CRV approach if we set $\Omega = \omega$. This means that Ω and ω^j do not have the same meaning, which is not too surprising, considering that ω^j is just an auxiliary local field in the CRV construction, while Ω is the angular velocity seen by observers at infinity.

The above observations can be used to estimate the angular velocity seen by observers at infinity when using the CRV approach for single stars. We first construct a single star using the CRV approach for a particular ω^j and compute its spin S_s. We then choose Ω such that the
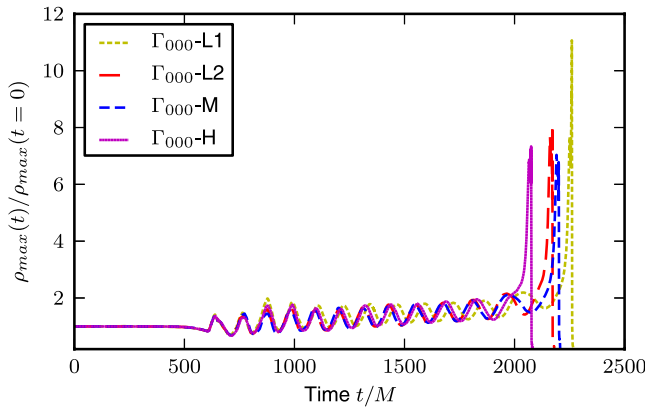
FIG. 11 (color online). Evolution of the maximum rest-mass density $\rho(t)$ (normalized by its initial value) for Γ_{000} using different resolutions.
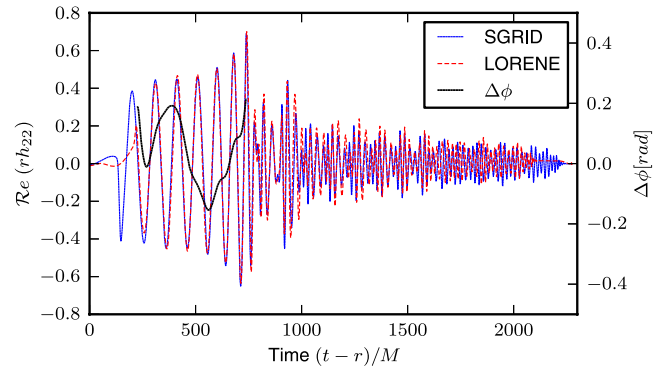

FIG. 12 (color online). GWs from runs with SGRID and Lorene initial data. Note that the two initial configurations have different separations. Shown is the $l = m = 2$ mode; the Lorene data are suitably shifted for the comparison. The black line refers to the phase difference up to merger.

corotating approach results in the same spin. We can then interpret this Ω as the angular velocity seen by observers at infinity for a single star with spin S_s. If we follow these steps for e.g. $\omega^z = 0.0046$, we find that we have to choose $\Omega = 0.0042$ to obtain the same spin with the corotating approach. Thus, the angular velocity seen at infinity for $\omega^z = 0.0046$ is really only 0.0042, which makes sense considering that any local frequency will be redshifted by the time it is observed at infinity. Thus, the spin period observed at infinity is about 10% larger than what we get from $2\pi/\omega^z$.

APPENDIX B: EQUILIBRIUM SEQUENCES

In this appendix, we present the equilibrium sequences of CRV data, considering in particular the curves $E(\ell)$, where $\ell = (J_{\rm ADM} - 2S_s)/(M_s^2 \nu)$, and $E = (M_{\rm ADM}/M_s - 1)/\nu$; see also Eqs. (12) and (13). The numerical data are again compared to PN and EOB [66] results, as described in the main text.

In Fig. 10, we report the curves $E(\ell)$ for sequences with $\omega^z = 0, \pm0.0023$. The 3 PN and adiabatic EOB curve are very close to the data for large separations. The differences are quantified in the right panel, by plotting $\Delta E = E - E^X$ with $X = 3$ PN, EOB. For the closest separation computed, the sequences equally deviate from EOB and 3 PN curves, but while the 3 PN result predicts a less bound binary, the EOB method predicts a more bound one. Note also a systematic difference in ΔE for different spins.

APPENDIX C: ROBUSTNESS OF SIMULATIONS IN THE POSTMERGER PHASE

The accuracy of the simulations in the orbital phase has been studied in different recent works. In particular, Refs. [16,50] presented the first convergence tests of waveforms' phase and amplitude in three- and nine-to-ten-orbit inspirals. We do not repeat that analysis here. The same works pointed out that after merger, convergence cannot be monitored in the waveforms and, in general, the results are much more dependent on the resolution and grid setup employed. See also Ref. [97] for similar conclusions obtained with other codes. In this appendix, we discuss the robustness of the simulations in the postmerger phase, in particular regarding the merger remnant, i.e. HMNS. We consider two different series of tests: (i) an *internal* test based on a resolution study and different grid setup, and (ii) an *external* test that compares the same evolution of similar initial data obtained with SGRID and Lorene. We focus on the irrotational configuration.

Fig. 11 shows the evolution of the maximum rest-mass density on the finest refinement level for the different resolutions considered in this work (see Table II). The results show a converging behavior of this quantity with increasing resolution, making us confident that the chosen setup gives, at least qualitatively, correct results. As observed in previous works, it is impossible to prove strict convergence either in this quantity or in the waveforms.

Extensive tests in an early stage of the work have shown that the nonconservative mesh refinement of BAM is not optimal for long-term evolution of the HMNS. During the inspiral, the compact stars are contained and completely resolved in a single Cartesian box at the finest refinement level. In the postmerger phase, however, a significant amount of matter *can* cross grid boundaries, unsurprisingly leading to severe violations of the rest-mass conservation. Only when the inner box encloses most matter can we expect systematic convergence.

As an example, we consider the grid configuration L2 and an equivalent configuration in which the number of points in the moving levels are reduced from $n^{\rm mv} = 144$ to $n^{\rm mv} = 96$ (but the same resolution is used). With smaller boxes, the outer layer of the HMNS are not covered by the finest refinement level. The larger mass violation of the setup with $n^{\rm mv} = 96$ led to *earlier* (in this case study) black hole formation by about $\Delta t \sim 700\,M$. Note, however, that the rest mass is conserved for the L2 grid up to $\sim$2% to collapse, while for the H grid it is up to $\sim$0.8%.

In a second series of tests, we compare the evolutions obtained with the SGRID initial data with Lorene data [98]. The Lorene data considered here have been employed in several works in the past, e.g. Refs. [50,97]. The initial separation slightly differs in the two cases: the proper distance is ~13.3 M for SGRID data and ~13.0 M for Lorene data. Lorene data employ four domains, and the number of collocation points for each domain is $N = 33 \times 25 \times 24$. SGRID uses four compactified domains with $N = 24 \times 24 \times 8$ points and two Cartesian domains with $N = 20 \times 20 \times 20$. The grid configuration used for the evolution in BAM is H.

Figure 12 shows the $l = m = 2$ waveforms aligned before merger on the time window $t/M \in [250, 739]$ (support of the black line.) The waveforms are very similar; phase differences (black line) are below $\Delta\phi \lesssim \pm 0.2$ rad. This uncertainty is of the same order of magnitude of a conservative error bar estimated from convergence tests. On the other hand, the HMNSs collapse within 150 M (2 ms) of each other.

We conclude that the results consistently approach a continuum limit when smaller grid spacings and sufficiently large boxes are employed. Results from different initial data are also consistent. However, care should be taken considering HMNS simulations of several milliseconds, since relatively small mass violations can lead to quantitatively different behaviors. We have tested different grid setups, grid resolutions, and independent initial data (when possible). Based on these results, we expect an uncertainty on the HMNS lifetime up to a maximum of 300 M, which is considerably shorter than the difference between model Γ_{000} and Γ_{050}^{++}. Although not commonly used in numerical relativity, a conservative AMR [99] is desirable; see Refs. [100,101] for the first recent applications in the field.

[1] D. R. Lorimer, Living Rev. Relativity **11,** 8 (2008).

[2] A. G. Lyne, M. Burgay, M. Kramer, A. Possenti, R. Manchester et al., Science **303,** 1153 (2004).

[3] M. Burgay, N. D'Amico, A. Possenti, R. Manchester, A. Lyne et al., Nature (London) **426,** 531 (2003).

[4] W. Tichy, Phys. Rev. D **84,** 024041 (2011).

[5] T. Damour, A. Nagar, and L. Villain, Phys. Rev. D **85,** 123007 (2012).

[6] D. A. Brown, I. Harry, A. Lundgren, and A. H. Nitz, Phys. Rev. D **86,** 084017 (2012).

[7] M. Hannam, D. A. Brown, S. Fairhurst, C. L. Fryer, and I. W. Harry, Astrophys. J. **766,** L14 (2013).

[8] K.-W. Lo and L.-M. Lin, Astrophys. J. **728,** 12 (2011).

[9] M. D. Duez, Y. T. Liu, S. L. Shapiro, and B. C. Stephens, Phys. Rev. D **69,** 104030 (2004).

[10] J. Abadie et al. (LIGO and Virgo collaborations), Classical Quantum Gravity **27,** 173001 (2010).

[11] J. Aasi et al. (LIGO and Virgo collaborations), arXiv:1304.0670.

[12] P. Ajith, Phys. Rev. D **84,** 084037 (2011).

[13] J. S. Read, C. Markakis, M. Shibata, K. Uryū, J. Creighton, and J. Friedman, Phys. Rev. D **79,** 124033 (2009).

[14] W. Del Pozzo, T. G. F. Li, M. Agathos, C. V. D. Broeck, and S. Vitale, Phys. Rev. Lett. **111,** 071101 (2013).

[15] L. Baiotti, T. Damour, B. Giacomazzo, A. Nagar, and L. Rezzolla, Phys. Rev. D **84,** 024017 (2011).

[16] S. Bernuzzi, M. Thierfelder, and B. Brügmann, Phys. Rev. D **85,** 104030 (2012).

[17] S. Bernuzzi, A. Nagar, M. Thierfelder, and B. Brügmann, Phys. Rev. D **86,** 044030 (2012).

[18] K. Hotokezaka, K. Kyutoku, and M. Shibata, Phys. Rev. D **87,** 044001 (2013).

[19] T. Baumgarte, G. Cook, M. Scheel, S. Shapiro, and S. Teukolsky, Phys. Rev. Lett. **79,** 1182 (1997).

[20] G. Mathews, P. Marronetti, and J. Wilson, Phys. Rev. D **58,** 043003 (1998).

[21] P. Marronetti, G. Mathews, and J. Wilson, Phys. Rev. D **58,** 107503 (1998).

[22] S. Bonazzola, E. Gourgoulhon, and J.-A. Marck, Phys. Rev. Lett. **82,** 892 (1999).

[23] P. Marronetti, G. Mathews, and J. Wilson, Phys. Rev. D **60,** 087301 (1999).

[24] K. Uryu and Y. Eriguchi, Phys. Rev. D **61,** 124023 (2000).

[25] K. Taniguchi and E. Gourgoulhon, Phys. Rev. D **66,** 104019 (2002).

[26] K. Uryu, F. Limousin, J. L. Friedman, E. Gourgoulhon, and M. Shibata, Phys. Rev. Lett. **97,** 171101 (2006).

[27] K. Uryu, F. Limousin, J. L. Friedman, E. Gourgoulhon, and M. Shibata, Phys. Rev. D **80,** 124004 (2009).

[28] L. Bildsten and C. Cutler, Astrophys. J. **400,** 175 (1992).

[29] Y. Sekiguchi, K. Kiuchi, K. Kyotoku, and M. Shibata, Phys. Rev. Lett. **107,** 051102 (2011).

[30] Y. Sekiguchi, K. Kiuchi, K. Kyotoku, and M. Shibata, Phys. Rev. Lett. **107,** 211101 (2011).

[31] C. Palenzuela, L. Lehner, M. Ponce, S. L. Liebling, M. Anderson, D. Neilsen, and P. Motl, Phys. Rev. Lett. **111,** 061105 (2013).

[32] R. Gold, S. Bernuzzi, M. Thierfelder, B. Brügmann, and F. Pretorius, Phys. Rev. D **86,** 121501 (2012).

[33] W. E. East and F. Pretorius, Astrophys. J. **760,** L4 (2012).

[34] J. A. Faber and F. A. Rasio, Living Rev. Relativity **15,** 8 (2012).

[35] W. Tichy, Phys. Rev. D **86,** 064024 (2012).

[36] P. Marronetti and S. L. Shapiro, Phys. Rev. D **68,** 104024 (2003).

[37] T. W. Baumgarte and S. L. Shapiro, Phys. Rev. D **80,** 064009 (2009).

[38] T. Damour, A. Nagar, D. Pollney, and C. Reisswig, Phys. Rev. Lett. **108,** 131101 (2012).

[39] M. Shibata and K. Uryu, Phys. Rev. D **61**, 064001 (2000).
[40] R. Oechslin and H. T. Janka, Phys. Rev. Lett. **99**, 121102 (2007).
[41] W. Kastaun, F. Galeazzi, D. Alic, L. Rezzolla, and J. A. Font, Phys. Rev. D **88**, 021501 (2013).
[42] P. Tsatsin and P. Marronetti, Phys. Rev. D **88**, 064060 (2013).
[43] J. Wilson and G. Mathews, Phys. Rev. Lett. **75**, 4161 (1995).
[44] J. Wilson, G. Mathews, and P. Marronetti, Phys. Rev. D **54**, 1317 (1996).
[45] J. W. York, Jr., Phys. Rev. Lett. **82**, 1350 (1999).
[46] W. Tichy, Phys. Rev. D **74**, 084005 (2006).
[47] W. Tichy, Classical Quantum Gravity **26**, 175018 (2009).
[48] W. Tichy, Phys. Rev. D **80**, 104034 (2009).
[49] B. Walther, B. Brügmann, and D. Müller, Phys. Rev. D **79**, 124040 (2009).
[50] M. Thierfelder, S. Bernuzzi, and B. Brügmann, Phys. Rev. D **84**, 044012 (2011).
[51] B. Brügmann, J. A. Gonzalez, M. Hannam, S. Husa, U. Sperhake, and W. Tichy, Phys. Rev. D **77**, 024027 (2008).
[52] B. Brügmann, W. Tichy, and N. Jansen, Phys. Rev. Lett. **92**, 211101 (2004).
[53] B. Brügmann, Int. J. Mod. Phys. D **08**, 85 (1999).
[54] T. Nakamura, K. Oohara, and Y. Kojima, Prog. Theor. Phys. Suppl. **90**, 1 (1987).
[55] M. Shibata and T. Nakamura, Phys. Rev. D **52**, 5428 (1995).
[56] T. W. Baumgarte and S. L. Shapiro, Phys. Rev. D **59**, 024007 (1999).
[57] C. Bona, J. Massó, J. Stela, and E. Seidel, in *The Seventh Marcel Grossmann Meeting: On Recent Developments in Theoretical and Experimental General Relativity, Gravitation, and Relativistic Field Theories*, edited by R. T. Jantzen, G. M. Keiser, and R. Ruffini (World Scientific, Singapore, 1996).
[58] M. Alcubierre, B. Brügmann, P. Diener, M. Koppitz, D. Pollney, E. Seidel, and R. Takahashi, Phys. Rev. D **67**, 084023 (2003).
[59] J. R. van Meter, J. G. Baker, M. Koppitz, and D.-I. Choi, Phys. Rev. D **73**, 124011 (2006).
[60] M. Thierfelder, S. Bernuzzi, D. Hilditch, B. Brügmann, and L. Rezzolla, Phys. Rev. D **83**, 064022 (2011).
[61] R. Borges, M. Carmona, B. Costa, and W. S. Don, J. Comput. Phys. **227**, 3191 (2008).
[62] M. J. Berger and J. Oliger, J. Comput. Phys. **53**, 484 (1984).
[63] C. Reisswig and D. Pollney, Classical Quantum Gravity **28**, 195015 (2011).
[64] T. Damour, Phys. Rev. D **64**, 124013 (2001).
[65] M. Campanelli, C. Lousto, and Y. Zlochower, Phys. Rev. D **74**, 041501 (2006).
[66] A. Buonanno and T. Damour, Phys. Rev. D **59**, 084006 (1999).
[67] A. Buonanno and T. Damour, Phys. Rev. D **62**, 064015 (2000).
[68] A. Nagar, Phys. Rev. D **84**, 084028 (2011).
[69] L. E. Kidder, C. M. Will, and A. G. Wiseman, Phys. Rev. D **47**, R4183 (1993).
[70] L. E. Kidder, Phys. Rev. D **52**, 821 (1995).
[71] H. Tagoshi, A. Ohashi, and B. J. Owen, Phys. Rev. D **63**, 044006 (2001).
[72] L. Blanchet, T. Damour, G. Esposito-Farese, and B. R. Iyer, Phys. Rev. Lett. **93**, 091101 (2004).
[73] G. Faye, L. Blanchet, and A. Buonanno, Phys. Rev. D **74**, 104033 (2006).
[74] T. Damour, P. Jaranowski, and G. Schäfer, Phys. Rev. D **77**, 064032 (2008).
[75] J. Steinhoff, S. Hergt, and G. Schäfer, Phys. Rev. D **77**, 081501 (2008).
[76] T. Damour, P. Jaranowski, and G. Schäfer, Phys. Rev. D **62**, 084011 (2000).
[77] E. Barausse, A. Buonanno, and A. Le Tiec, Phys. Rev. D **85**, 064010 (2012).
[78] T. Damour, A. Nagar, and S. Bernuzzi, Phys. Rev. D **87**, 084035 (2013).
[79] D. Bini and T. Damour, Phys. Rev. D **87**, 121501 (2013).
[80] Y. Pan, A. Buonanno, A. Taracchini, L. E. Kidder, A. H. Mroue, H. P. Pfeiffer, M. A. Scheel, and B. Szilágyi, Phys. Rev. D **89**, 084006 (2014).
[81] T. Damour, P. Jaranowski, and G. Schäfer, Phys. Rev. D **78**, 024009 (2008).
[82] S. Balmelli and P. Jetzer, Phys. Rev. D **87**, 124036 (2013).
[83] V. Paschalidis, Z. B. Etienne, and S. L. Shapiro, Phys. Rev. D **86**, 064032 (2012).
[84] K. Hotokezaka, K. Kiuchi, K. Kyutoku, T. Muranushi, Y.-i. Sekiguchi, M. Shibata, and K. Taniguchi, Phys. Rev. D **88**, 044026 (2013).
[85] M. B. Deaton, M. D. Duez, F. Foucart, E. O'Connor, C. D. Ott, L. E. Kidder, C. D. Muhlberger, M. A. Scheel, and B. Szilagyi, Astrophys. J. **776**, 47 (2013).
[86] N. Stergioulas, A. Bauswein, K. Zagkouris, and H.-T. Janka, arXiv:1105.0368.
[87] L. Baiotti, S. Bernuzzi, G. Corvino, R. De Pietri, and A. Nagar, Phys. Rev. D **79**, 024002 (2009).
[88] H. Dimmelmeier, N. Stergioulas, and J. A. Font, Mon. Not. R. Astron. Soc. **368**, 1609 (2006).
[89] A. Bauswein and H.-T. Janka, Phys. Rev. Lett. **108**, 011101 (2012).
[90] F. Foucart, L. Buchman, M. D. Duez, M. Grudich, L. E. Kidder, I. MacDonald, A. Mroue, H. P. Pfeiffer, M. A. Scheel, and B. Szilagyi, Phys. Rev. D **88**, 064017 (2013).
[91] S. Bernuzzi, A. Nagar, S. Balmelli, T. Dietrich, and M. Ujevic, arXiv:1402.6244 [Phys. Rev. Lett. (to be published)].
[92] P. Ajith, M. Hannam, S. Husa, Y. Chen, B. Brügmann *et al.*, Phys. Rev. Lett. **106**, 241101 (2011).
[93] M. Hannam, S. Husa, F. Ohme, D. Müller, and B. Brügmann, Phys. Rev. D **82**, 124008 (2010).
[94] L. Santamaria, F. Ohme, P. Ajith, B. Brügmann, N. Dorband *et al.*, Phys. Rev. D **82**, 064016 (2010).
[95] M. Hannam, S. Husa, B. Brügmann, and A. Gopakumar, Phys. Rev. D **78**, 104007 (2008).
[96] M. Favata, Phys. Rev. Lett. **112**, 101101 (2014).
[97] L. Baiotti, B. Giacomazzo, and L. Rezzolla, Classical Quantum Gravity **26**, 114005 (2009).
[98] Eric Gourgoulhon, Philippe Grandclément, Jean-Alain Marck, Jérôme Novak, and Keisuke Taniguchi, Paris Observatory, Meudon section—LUTH laboratory, http://www.lorene.obspm.fr/.
[99] M. J. Berger and P. Colella, J. Comput. Phys. **82**, 64 (1989).
[100] W. E. East, F. Pretorius, and B. C. Stephens, Phys. Rev. D **85**, 124010 (2012).
[101] C. Reisswig, R. Haas, C. Ott, E. Abdikamalov, P. Mösta, D. Pollney, and E. Schnetter, Phys. Rev. D **87**, 064023 (2013).